

NOVEMBER 11 2025

High-resolution sonar imaging based on wideband fast iterative shrinkage thresholding deconvolution beamforming



Deyue Hong; Zhiwen Qian; Xiaomei Fu; Yi Zhu; Seiji Adachi; Chenghao Hu; Ge Dai; Jingsheng Zhai



J. Acoust. Soc. Am. 158, 3744–3757 (2025)

<https://doi.org/10.1121/10.0039861>



View
Online



Export
Citation

Articles You May Be Interested In

Bayesian-driven cyclic-cross-spectral matrix completion: Non-synchronous measurements for cyclostationary acoustic sources

J. Acoust. Soc. Am. (October 2025)

Deblurring of images using novel artificial neural network (ANN) algorithm to enhance the accuracy and comparing with Richardson-Lucy deconvolution algorithm (RLD)

AIP Conf. Proc. (November 2023)

Enhancement of accuracy and specificity in image using novel deblurring method with support vector machine (SVM) compared by Richardson-Lucy deconvolution algorithm

AIP Conf. Proc. (March 2024)

High-resolution sonar imaging based on wideband fast iterative shrinkage thresholding deconvolution beamforming

Deyue Hong,¹ Zhiwen Qian,^{1,a)} Xiaomei Fu,¹ Yi Zhu,¹ Seiji Adachi,¹ Chenghao Hu,² Ge Dai,³ and Jingsheng Zhai¹

¹School of Marine Science and Technology, Tianjin University, Tianjin 300072, China

²The State Key Laboratory of Acoustics, Chinese Academy of Sciences, Beijing 100000, China

³Sapphireview Technologies, Zhuhai 519000, China

ABSTRACT:

Conventional beamforming (CBF) has been widely applied for underwater acoustic imaging owing to its robustness and low complexity. However, its resolution is limited by the Rayleigh threshold. Thus, various imaging deblurring methods, such as deconvolution beamforming, have been proposed to improve resolution without changing the array aperture. But these intensity-based methods require the targets to be incoherent and are based on the narrowband signals, which mismatches with practical sonar imaging model. In response, this study presents a matrix transformation and monotone fast iterative shrinkage thresholding algorithm (MFISTA) to extend deconvolution beamforming to wideband coherent signals for high-resolution imaging. Wherein the former focuses received signals to a reference frequency by the focusing signal subspace, which can reasonably approximate a broadband signal as a narrowband. Then the MFISTA develops a complex-domain deconvolution beamforming to theoretically remove the cross term interference generated by coherent targets in intensity-based methods. Simulations in uniform linear array demonstrate that the main lobewidth of the proposed method is less than 1/4 that of the CBF method and approximately 1/3 that of other CBFs, while its sidelobe level is over 5 dB lower than other methods. Lake-based imaging experiments validated that the proposed method has superior resolution, main-lobewidth, sidelobe level, and noise immunity compared to other intensity-based methods. © 2025 Acoustical Society of America. <https://doi.org/10.1121/10.0039861>

(Received 21 November 2024; revised 29 August 2025; accepted 11 October 2025; published online 11 November 2025)

[Editor: James F. Lynch]

Pages: 3744–3757

I. INTRODUCTION

Imaging sonar has been widely applied in recent decades for underwater vehicle navigation and obstacle avoidance, underwater target detection, and pipeline monitoring.^{1–3} Generally, broadband signal-based conventional beamforming (CBF) is typically employed for two-dimensional (2D) imaging sonar because of its robustness and real-time performance. However, CBF is essentially an application of the time-domain Fourier transform in the spatial domain; therefore, its spatial resolutions are limited by the Rayleigh threshold, i.e., the presence of wide mainlobes and high-intensity sidelobes, resulting in limited imaging resolution and contrast.⁴

Various methods have been proposed to improve the imaging resolution and contrast based on CBF.⁵ Minimum variance distortionless response (MVDR)⁶ and the multiple signal classification^{7,8} can improve beamforming resolution, but it is necessary to know *a priori* information. The adaptive beamformer, which has narrower mainlobes and lower sidelobes than CBF, the premise requires a large number of array elements and a non-coherent environment.^{9–11} Compressed sensing can achieve high resolution using small aperture arrays but is limited by computational cost and signal-to-noise ratio (SNR).¹²

The deconvolution method, derived from the theory of mathematical inverse problems, is widespread in several fields because of its superior resolution, excellent robustness, and noise immunity. Many deconvolution algorithms such as the deconvolution approach for the mapping of acoustic sources (DAMAS),¹³ non-negative least-squares (NNLS),¹⁴ CLEAN,¹⁵ Richardson-Lucy (RL),¹⁶ etc., have been developed based on the assumption that the targets are non-coherent, which results in a mismatch with the actual multi-phase coherent imaging model. Wherein DAMAS performs matrix inversion, which can result in false sources at close distances and high computational complexity. NNLS does not require the point spread function (PSF) to be translation-invariant, but it is sensitive to noise. In addition, the shortcomings of the CLEAN and DAMAS algorithms are that they assume that the sound source is composed of PSFs, making them applicable only to a few point sources. RL is suitable for PSF translation-invariant deconvolution problems and has lower side lobes and narrower main lobes. In recent years, deconvolution beamforming has been adopted to underwater acoustic measurements to improve beam resolution. This is because the beam results can be expressed as a convolution of the underwater targets and the PSF. By deconvolving the CBF beamformer map, the distribution of the actual targets can be obtained with a clean beam map, thus improving the target resolution with spatial distribution. Yang employed the deconvolution

^{a)}Email: zhiwenqian@tju.edu.cn

beamforming to estimate the DOA of the ULA, achieving narrower mainlobe width and lower sidelobes level than MVDR, and preserving the robustness of CBF.¹⁷ Subsequently, it is applied to non-uniform linear arrays,¹⁸ vector arrays,¹⁹ circular arrays,²⁰ and coprime arrays,²¹ which suggests that deconvolution beamforming has a wide range of array applicability. Huang *et al.*²² proposed a fast deconvolution beamforming algorithm to reduce the computation complexity of the RL algorithm and selected it to the imaging sonar. Ma *et al.*²³ employed a multi-beam (MB) orthogonal frequency division multiplexing based on RL deconvolved for underwater acoustic communication, which capitalizes on multipath diversity gain achieved by combining MB outputs originating from various arrival angles. Due to the PSF of the array in the near field is shift-variant, Sun *et al.*²⁴ presented an extended Richardson-Lucy (Ex-RL) algorithm to underwater acoustic imaging. Wang *et al.*²⁵ formulated the three-dimensional (3D) beamforming outputs as a convolution of the beam pattern and the scattering function of targets and performed the deconvolution beamforming for 3D imaging on the 2D array. Similar to deconvolution beamforming, Liu *et al.*²⁶ proposed a deconvolution method to improve range resolutions and suppress range sidelobes for sonar imaging using stepped-frequency pulses. Then, a two-step deconvolution method based on distance and azimuth in active imaging sonar was proposed.^{27–29} In the first step, the deconvolution method is applied to the angular dimension; in the second step, the deconvolution method is applied to the range dimension where the auto-correlation function of the transmitted linear frequency modulation pulse is taken as the PSF. These methods have improved the resolution of acoustic images.

However, most of the aforementioned deconvolution methods aim at intensity deconvolution beamforming, adopting the assumption that the targets are incoherent and the signal is narrowband. In deconvolution of the CBF results generated by coherent targets, these intensity-based methods suffer from mismatch with real targets and weakened sidelobe suppression ability.³⁰ Unfortunately, for imaging sonar, this assumption is challenging because the signals reflected by the targets are inherently coherent. At the same time, considering noise immunity and improved ranging accuracy for transmission in underwater environments, wideband signals are often used as underwater transmission signals. In this case, although some complex-value deconvolution methods have been proposed to improve the DOA estimation of the coherent signals³¹ and beamforming performance,³² the signals are also assumed to be narrowband and have not been applied to imaging sonar.³³

In response, the MT-MFISTA for high-resolution imaging sonar is proposed in this study. The focusing signal subspace (FSS) is introduced for wideband signal-based beamforming, the covariance matrix at each frequency is transformed to the focusing covariance matrix at the reference focusing frequency by using the focusing matrix transformation. Then the MFISTA develops a complex-domain deconvolution beamforming to theoretically avoid the cross

term interference generated by coherent targets in intensity-based methods. Finally, the sidelobe amplitude is suppressed and the mainlobe resolution is improved by this deconvolution beamforming of wideband coherent signals, which in turn achieves higher resolution and contrast in acoustic imaging. The contributions of the study are as follows:

- The problem that the traditional deconvolution algorithm does not apply to coherent target imagining is solved by the MFISTA, which was implemented in the complex domain to avoid cross terms and reconstruct the convolutional relationship between CBF output and targets.
- The deconvolution beamforming method is expanded to the wideband signal case by matrix transformation, which focus the wideband signal to a reference frequency, making it more adaptable to practical hydroacoustic applications.
- Simulations and experiments performed on the ULA have demonstrated that MT-MFISTA has advantages in the terms of mainlobe width, sidelobe level, noise immunity, and image quality.

The MT-MFISTA is proposed in this paper for high-resolution imaging of broadband coherent targets. Wherein the CBF output results are deconvolved in the complex domain and avoids the coherence associated with the square of the energy spectrum caused in other intensity-based deconvolutions, achieving accurate azimuth estimation of coherent targets. At the same time, broadband signals are reasonably divided into subbands in the frequency domain and focusing them onto the reference frequency using a focusing matrix of the FSS. Ultimately, high-resolution sonar imaging is achieved. This proposed MT-MFISTA is applicable to ocean acoustics related to array coherent signal processing, such as underwater acoustic positioning, imaging, and communication.

The rest of this article is composed as follows. Section II describes the signal model and intensity-based deconvolution beamforming. Section III introduces a wideband coherent target imaging method based on MT-MFISTA. Sections IV and V show the performance of the proposed method by simulations and experiments. Finally, Sec. VI concludes this article.

II. DECONVOLUTION BEAMFORMING

A. Sonar imaging model

The imaging sonar can be simplified as a transmitter and a hydrophone array, and the imaging model is shown in Fig. 1. Typically, the sonar transmits a single wide beam to illuminate the imaging area and uses the receiving array to obtain echo signals and generate multiple narrow beams. It is assumed that the receiving array is a ULA containing M elements, and the spacing between each element is d . Considering that the transmitted signal is narrowband, and there are k targets from the far field in the acoustic coverage area. The echo signal reflected from the k th target is incident to the receiving array with direction θ_k . Taking the first element as a reference, the signal received at the m th element can be represented as

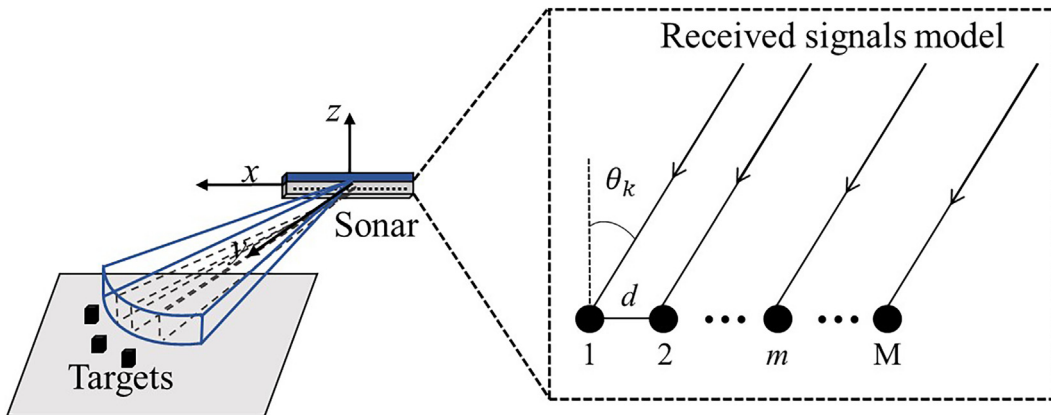


FIG. 1. Sonar imaging model and received signals model.

$$x_m(t) = \sum_{k=1}^K s_k(t - \tau_{m,k}) + n_m(t), \quad (1)$$

where $s_k(t)$ is the reflected signal of the k th target received by the reference element, $k = 1, 2, \dots, K$; $n_m(t)$ represents noise and is not related to the targets, $\tau_{m,k}$ is the time delay between the m th element and the reference of the k th target signal, which is represented as

$$\tau_{m,k} = \frac{(m-1)d \sin \theta_k}{c}, \quad (2)$$

where c is the sound speed in water.

Since the signal is narrowband, the time delay can be equated to a phase shift, thus Eq. (1) can be rewritten as

$$x_m(t) = \sum_{k=1}^K [a_m(\theta_k) \cdot s_k(t)] + n_m(t), \quad (3)$$

where $a_m(\theta_k) = e^{-j2\pi f \tau_{m,k}}$, f is the frequency of the signal, and complex $j = \sqrt{-1}$.

Thus, the array received signal model of ULA is expressed in the following matrix form:

$$\mathbf{X} = \mathbf{A}(\theta) \mathbf{S} + \mathbf{N}, \quad (4)$$

where $\mathbf{S} \in \mathbb{C}^K$ represents the complex-valued vector consisting of the reflected signals of K targets, $\mathbf{N} \in \mathbb{C}^M$ is the noise received by M elements, and $\mathbf{A}(\theta) \in \mathbb{C}^{M \times K}$ is the look-direction matrix. The k th column of $\mathbf{A}(\theta)$ corresponds to the direction vector of the k th target in the direction θ_k , defined as follows:

$$\begin{aligned} \mathbf{a}_k &= [a_{k1}, \dots, a_{km}, \dots, a_{kM}]^T, \\ a_{km} &= e^{-j2\pi(m-1)f d \sin \theta_k / c}, \end{aligned} \quad (5)$$

where the superscript $[]^T$ denotes the matrix transpose.

B. Intensity-based deconvolution beamforming

To estimate the direction of the signal, the steering vector is constructed to compensate for the time delay in the

CBF. For the desired direction ϑ , the steering vector $\omega(\vartheta) \in \mathbb{C}^M$ can be expressed as

$$\begin{aligned} \omega(\vartheta) &= [\omega_1, \dots, \omega_m, \dots, \omega_M]^T, \\ \omega_m &= \frac{1}{M} e^{-j2\pi(m-1)f d \sin \vartheta / c}. \end{aligned} \quad (6)$$

Ignoring the noise term, the CBF output of the desired direction ϑ is obtained as follows:

$$\begin{aligned} y(\vartheta) &= \omega^H(\vartheta) \mathbf{X} \\ &= \sum_{k=1}^K \frac{s_k}{M} \sum_{m=1}^M e^{j2\pi f (m-1) d (\sin \vartheta - \sin \theta_k) / c} \\ &= \sum_{k=1}^K s_k e^{j\pi f (M-1) d \mu_k / c} \frac{\sin c(M \pi f d \mu_k / c)}{\sin c(f \pi d \mu_k / c)}, \end{aligned} \quad (7)$$

where the superscript $.^H$ denotes the conjugate transpose and $\mu_k = \sin \vartheta - \sin \theta_k$. Clearly, $y(\vartheta)$ can be regarded as the superposition of K targets in the direction ϑ through the PSF.

In addition, the beamforming intensity in direction ϑ can be expressed as follows:

$$\begin{aligned} B(\vartheta) &= |y(\vartheta)|^2 \\ &= \sum_{k=1}^K \left| \frac{\sin c(M \pi f d \mu_k / c)}{\sin c(\pi f d \mu_k / c)} \right|^2 |s_k|^2 + \sum_{k=1}^K \sum_{l=1, l \neq k}^K C_{kl}, \\ C_{kl} &= s_k s_l^* e^{[j\pi f (M-1) d / c] (\mu_k - \mu_l)} \frac{\sin c(M \pi f d \mu_k / c)}{\sin c(\pi f d \mu_k / c)} \\ &\quad \times \frac{\sin c(M \pi f d \mu_l / c)}{\sin c(\pi f d \mu_l / c)}, \end{aligned} \quad (8)$$

where $|\cdot|$ denotes the modulo and the superscript $.^*$ denotes the conjugate. Notably, When and only when the targets are incoherent, the sum of the cross-terms C_{kl} can be neglected. In this case, Eq. (8) can be simplified to

$$B(\vartheta) = \sum_{k=1}^K \left| \frac{\sin c(M \pi f d \mu_k / c)}{\sin c(\pi f d \mu_k / c)} \right|^2 |s_k|^2. \quad (9)$$

Remarkably, Eq. (9) can be rewritten in an integral form as the convolution of the PSF with the target intensity distribution¹⁹

$$B(\sin \vartheta) = \int_{-1}^1 B_{\text{psf}}(\sin \vartheta - \sin \theta) S(\sin \theta) d\sin \theta, \quad (10)$$

where B_{psf} is real-value PSF, which is expressed in terms of the sine of the direction angle and is shift invariant

$$B_{\text{psf}}(x) = \left| \frac{\text{sinc}(M\pi f dx/c)}{\text{sinc}(\pi f dx/c)} \right|^2. \quad (11)$$

The distribution of the targets is given by $S(\sin \theta) = \sum_{k=1}^K |s_k|^2 \delta(\sin \theta - \sin \theta_k)$.

Considering that the azimuth of the beam scanning is discrete and finite in practice, all the scanning azimuths in the imaging area can be expressed in the form of matrix multiplication of Eq. (12),

$$\mathbf{B} = \mathbf{B}_p \mathbf{S}_B. \quad (12)$$

$B(\sin \vartheta)$ and $S(\sin \theta)$ can be regarded as the elements in \mathbf{B} and \mathbf{S}_B , respectively. \mathbf{B}_p is a square matrix, each column corresponding to a PSF in a certain direction ϑ in space. In addition, positive definite constraint needs to be added because all elements are positive.

Intensity-based deconvolution beamforming methods, such as DAMAS, NNLS, RL, etc., are proposed based on the assumption that the target echo signal is incoherent. However, when the targets are coherent, the cross-terms derived from signal intensity cannot be ignored, and then the convolutional model built according to Eq. (9) will be mismatched, making the results deviate from the real situation. Furthermore, the equations are derived for narrowband signals and do not apply to the wideband case. To overcome the above limitations, a new deconvolution beamforming method for wideband coherent signals is proposed in Sec. III.

III. PROPOSED MT-MFISTA

As previously mentioned, the imaging sonar employs wideband signals as acoustic transmitting, and the received signals reflected by the targets are coherent. Thus, the intensity-based deconvolution beamforming methods assume that the echo signals are incoherent, which suffers from the problem of model mismatch and leads to degradation of imaging quality. In response, we propose the MT-MFISTA for the case where the sonar signals are coherent and wideband. First, the received wideband signal is divided into subbands of different frequencies and focused on a reference frequency by matrix transformation for CBF output. Second, a more precise azimuthal distribution of the target is reconstructed by the MFISTA. Third, the target distance information is obtained by pulse compression and together with the azimuthal angle to generate high-resolution sonar images. The detailed flow chart of the proposed method is shown in Fig. 2.

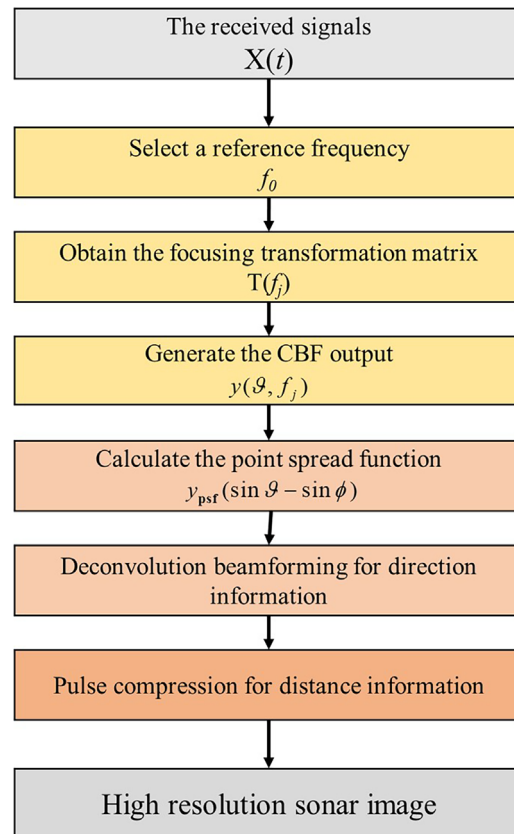


FIG. 2. Flowchart of the proposed method.

A. Wideband signal-based beamforming

To overcome the significant performance degradation caused by traditional methods that directly equate broadband signals to multiple subbands. The FSS is introduced to reasonably approximate a wideband signal as many narrowband signals.³⁴ A matrix transformation (MT) combines the eigenvector of signal subspace of the reference frequency and the eigenvector of signal subspace of other discrete frequencies with the constraint of Frobenius norm. In general, the center frequency of the wideband signal is selected as the reference frequency. Here, to keep the equivalent performance of broadband signals based on the FSS algorithm, it is best to avoid low-sample small snapshots.

Before determining the focusing matrix, the target direction should first be estimated to define the array manifold matrices at different frequencies. Then, through focusing transformation, the data across all frequencies can be aligned to the reference frequency. Assuming that the focusing transformation matrix for the j th frequency point is denoted as $\mathbf{T}(f_j)$, then the following equation holds:

$$\mathbf{T}(f_j)\mathbf{A}(f_j) = \mathbf{A}(f_0), \quad (13)$$

where f_j is the j th frequency point and f_0 is the reference frequency. The received signal after matrix transformation in the frequency can be expressed as

$$\mathbf{T}(f_j)\mathbf{X}(f_j) = \mathbf{T}(f_j)\mathbf{A}(f_j)\mathbf{S}(f_j). \quad (14)$$

The key to realizing the transformation relationship is to construct a suitable focus transformation matrix that minimizes the error between the $\mathbf{A}(f_0)$ and $\mathbf{T}(f_j)\mathbf{A}(f_j)$. The error can be constrained by the Frobenius-norm in FSS algorithms

$$\min_{\mathbf{T}(f_j)} \|\mathbf{A}(f_0) - \mathbf{T}(f_j)\mathbf{A}(f_j)\|_F^2, \quad (15)$$

where $\mathbf{T}(f_j)$ is a unitary matrix that satisfies $\mathbf{T}^H(f_j)\mathbf{T}(f_j) = \mathbf{I}$. To construct the focusing transformation matrix, Eq. (15) can be rewritten as follows:

$$\begin{aligned} & \|\mathbf{A}(f_0) - \mathbf{T}(f_j)\mathbf{A}(f_j)\|_F^2 \\ &= \text{tr}\left\{\left[\mathbf{A}(f_0) - \mathbf{T}(f_j)\mathbf{A}(f_j)\right]\left[\mathbf{A}(f_0) - \mathbf{T}(f_j)\mathbf{A}(f_j)\right]^H\right\} \\ &= \text{tr}\left[\mathbf{A}(f_0)\mathbf{A}^H(f_0)\right] + \text{tr}\left[\mathbf{A}(f_j)\mathbf{A}^H(f_j)\right] \\ &\quad - 2\text{Re}\left\{\text{tr}\left[\mathbf{A}(f_0)\mathbf{A}^H(f_j)\mathbf{T}^H(f_j)\right]\right\}, \end{aligned} \quad (16)$$

where $\text{tr}(\cdot)$ is the trace of the matrix and $\text{Re}(\cdot)$ is the real part.

Obviously, the first two terms in Eq. (16) are fixed values, and to minimize this function, the last term needs to take the maximum value. Writing matrix \mathbf{P}_j as

$$\mathbf{P}_j = \mathbf{A}(f_0)\mathbf{A}^H(f_j). \quad (17)$$

By decomposing the singular values of the matrix, the matrix \mathbf{P}_j is given by

$$\mathbf{P}_j = \mathbf{U}_j \sum \mathbf{V}_j^H, \quad (18)$$

where matrices \mathbf{U}_j and \mathbf{V}_j are the left and right singular vector of matrix \mathbf{P}_j , $\sum = \text{diag}(\sigma_{11}, \sigma_{22}, \dots, \sigma_{MM})$, and σ_{ii} is the singular value of matrix \mathbf{P}_j . Assuming that the rank of the matrix \mathbf{P}_j is r , we can get

$$\sigma_{11} \geq \sigma_{22} \geq \dots \geq \sigma_{rr} > \sigma_{r+1,r+1} = \dots = \sigma_{MM} = 0. \quad (19)$$

Then the last term of Eq. (16) can be written as

$$\begin{aligned} \text{Re}\left\{\text{tr}\left[\mathbf{A}(f_0)\mathbf{A}^H(f_j)\mathbf{T}^H(f_j)\right]\right\} &\leq |\text{tr}(\mathbf{P}_j\mathbf{T}^H(f_j))| \\ &= \left| \text{tr}\left(\mathbf{U}_j \sum \mathbf{V}_j^H \mathbf{T}^H(f_j)\right) \right| \\ &= \left| \text{tr}\left(\sum \mathbf{V}_j^H \mathbf{T}^H(f_j) \mathbf{U}_j\right) \right|. \end{aligned} \quad (20)$$

Let $\mathbf{Q} = \mathbf{V}_j^H \mathbf{T}^H(f_j) \mathbf{U}_j$, \mathbf{Q} be a unitary matrix, $|\mathbf{Q}_{ii}| \leq 1, i = 1, 2, \dots, M$, and Eq. (20) becomes

$$\begin{aligned} \text{Re}\left\{\text{tr}\left[\mathbf{A}(f_0)\mathbf{A}^H(f_j)\mathbf{T}^H(f_j)\right]\right\} &\leq \left| \text{tr}\left(\sum \mathbf{Q}\right) \right| \\ &\leq \sum_{i=1}^M |\mathbf{Q}_{ii}| \sigma_{ii} \\ &\leq \sum_{i=1}^M \sigma_{ii}. \end{aligned} \quad (21)$$

When $|\mathbf{Q}_{ii}| = 1, i = 1, 2, \dots, M$, Eq. (21) obtains the maximum value. Then the solution of Eq. (15) is represented as

$$\mathbf{T}(f_j) = \mathbf{U}_j \mathbf{V}_j^H. \quad (22)$$

Then \mathbf{Q} can be given by

$$\begin{aligned} \mathbf{Q} &= \mathbf{V}_j^H \mathbf{T}^H(f_j) \mathbf{U}_j \\ &= \mathbf{V}_j^H (\mathbf{V}_j \mathbf{U}_j^H) \mathbf{U}_j = \mathbf{I} \\ &\text{object to } |\mathbf{Q}_{ii}| = 1, i = 1, 2, \dots, M. \end{aligned} \quad (23)$$

By bringing Eqs. (14) and (22) into Eq. (7), the CBF output result in the direction ϑ of the certain frequency point f_j can be obtained as follows:

$$\begin{aligned} y(\vartheta, f_j) &= \boldsymbol{\omega}^H(\vartheta, f_j) \mathbf{T}(f_j) \mathbf{X}(f_j) \\ &= \boldsymbol{\omega}^H(\vartheta, f_j) \mathbf{U}_j \mathbf{V}_j^H \mathbf{X}(f_j). \end{aligned} \quad (24)$$

B. MFISTA-based complex deconvolution beamforming

For intensity-based deconvolution methods, which is developed by the assumption that the targets are non-coherent and based on energy form Eq. (8), the coherent signals have cross-terms that cannot be ignored, which is the root cause of the degradation of beamforming model accuracy, and intensity-based deconvolution methods such as DAMAS, NNLS, RL, etc., mismatch with the actual multi-phase coherent imaging model. Based on non-square Eq. (7), we propose a method and perform deconvolution processing in the complex domain to avoid the effect of cross-terms, which are caused by the square operation in intensity-based deconvolutions. Thus, Eq. (7) can be rewritten in integral form as follows:

$$y(\sin \vartheta) = \int_{-1}^1 y_{\text{psf}}(\sin \vartheta - \sin \theta) s(\sin \theta) d \sin \theta, \quad (25)$$

where y_{psf} denotes the complex-valued PSF, which is shift-invariant for the sine of the angle.

$$y_{\text{psf}}(x) = e^{j\pi f(M-1)dx/c} \frac{\sin c(Mf\pi dx/c)}{\sin c(f\pi dx/c)}. \quad (26)$$

Considering that there are G scanning directions uniformly distributed in the imaging area $[\vartheta_1, \vartheta_2, \dots, \vartheta_G]$, then the CBF output for all scanning directions can be expressed in matrix form as

$$\mathbf{Y} = \mathbf{Y}_p \mathbf{S}_Y, \quad (27)$$

where $\mathbf{Y} \in \mathbb{C}^G$ is the output of CBF, $\mathbf{Y}_p \in \mathbb{C}^{G \times G}$ is the complex-valued matrix of point and $\mathbf{S}_Y \in \mathbb{C}^G$ is the spatial orientation of the targets. The above matrices are defined as follows:

$$\mathbf{Y} = [y(\sin \vartheta_1), y(\sin \vartheta_2), \dots, y(\sin \vartheta_G)]^T, \quad (28)$$

$$\mathbf{Y}_p = \begin{bmatrix} y_{psf}(\sin \vartheta_1 - \sin \phi_1) & y_{psf}(\sin \vartheta_1 - \sin \phi_2) & \cdots & y_{psf}(\sin \vartheta_1 - \sin \phi_G) \\ y_{psf}(\sin \vartheta_2 - \sin \phi_1) & y_{psf}(\sin \vartheta_2 - \sin \phi_2) & \cdots & y_{psf}(\sin \vartheta_2 - \sin \phi_G) \\ \vdots & \vdots & \ddots & \vdots \\ y_{psf}(\sin \vartheta_G - \sin \phi_1) & y_{psf}(\sin \vartheta_G - \sin \phi_2) & \cdots & y_{psf}(\sin \vartheta_G - \sin \phi_G) \end{bmatrix}, \quad (29)$$

$$\mathbf{S}_Y = [s(\sin \phi_1), s(\sin \phi_2), \dots, s(\sin \phi_G)]^T,$$

$$s(\sin \phi_g) = \begin{cases} s_k, & \theta_k = \phi_g, \\ 0, & \theta_k \neq \phi_g. \end{cases} \quad (30)$$

At this time, the deconvolution problem in Eq. (25) can be regarded as the estimation problem of \mathbf{S}_Y in Eq. (27). However, \mathbf{S}_Y is not an invertible matrix, and note that the distribution of targets is sparse for the scanning orientation, so the estimation of \mathbf{S}_Y can be achieved with a convex optimization model

$$\widehat{\mathbf{S}}_Y = \arg \min_{\mathbf{S}_Y} \frac{1}{2} \|\mathbf{Y}_p \mathbf{S}_Y - \mathbf{Y}\|_2^2 + \eta \|\mathbf{S}_Y\|_1, \quad (31)$$

where $\widehat{\mathbf{S}}_Y$ is the estimated value of \mathbf{S}_Y and η denotes the regularization coefficient that constrains the sparsity of the model. $\|\cdot\|_2$ denotes the ℓ_2 -norm and $\|\cdot\|_1$ denotes the ℓ_1 -norm.

Here, the MFISTA is used to solve Eq. (31), which is theoretically based on the proximal-gradient method for the solution, and paired with the Nesterov's algorithm for accelerated convergence. A Lipschitz constant for MFISTA is required, denoted as L . It is well known that for $f(\mathbf{S}_Y) = \frac{1}{2} \|\mathbf{Y}_p \mathbf{S}_Y - \mathbf{Y}\|_2^2 + \eta \|\mathbf{S}_Y\|_1$, a Lipschitz constant is the maximum eigenvalue of the Hessian matrix $\nabla^2 f(\mathbf{S}_Y) = \mathbf{Y}_p^H \mathbf{Y}_p$. The proximal-gradient operator computed of the Eq. (31) can be expressed as

$$q_i = ST_{\eta/L} \left(\frac{1}{L} \mathbf{Y}_p^H (\mathbf{Y} - \mathbf{Y}_p p_i) + p_i \right), \quad (32)$$

where $ST_{\eta/L}$ is the shrinkage-thresholding operator, which for any given complex vector $\mathbf{x} = [x_1, x_2, \dots, x_G]^T \in \mathbb{C}^G$ and real number η/L is defined as follows:

$$ST_{\eta/L}(x_g) = \begin{cases} 0, & |x_g| < \frac{\eta}{L}, \\ x_g - \frac{\eta}{L} \frac{x_g}{|x_g|}, & |x_g| \geq \frac{\eta}{L}. \end{cases} \quad (33)$$

To ensure monotonicity, the MFISTA requires the computation of a single function evaluation

$$\widehat{\mathbf{S}}_{Y,i} = \arg \min_{S \in \{q_i, \widehat{\mathbf{S}}_{Y,i-1}\}} \frac{1}{2} \|\mathbf{Y} - \mathbf{Y}_p S\|_2^2 + \eta \|S\|_1, \quad (34)$$

where $\widehat{\mathbf{S}}_{Y,i}$ ($i = 1, 2, \dots, I$) denotes the result of the i th iteration.

The iterative process and the scale of the momentum update can be expressed as follows:

$$l_{i+1} = \left(1 + \sqrt{1 + 4l_i^2} \right) / 2, \quad (35)$$

$$p_{i+1} = \widehat{\mathbf{S}}_{Y,i} + \frac{l_i - 1}{l_{i+1}} (\widehat{\mathbf{S}}_{Y,i} - \widehat{\mathbf{S}}_{Y,i-1}) + \frac{l_i}{l_{i+1}} (q_i - \widehat{\mathbf{S}}_{Y,i}), \quad (36)$$

where l_i , q_i and p_i are an intermediate variable in the iterative process and have no physical significance.

The initial value of the iteration is set as $p_1 = \mathbf{Y}$, $l_1 = 1$. When $|\widehat{\mathbf{S}}_{Y,i+1} - \widehat{\mathbf{S}}_{Y,i}| < \epsilon$ or i reaches the maximum number of iterations, the iteration ends and $\widehat{\mathbf{S}}_{Y,i+1}$ indicates the result of the MFISTA.

C. The value of the regularization coefficient

A suitable selection of regularization coefficients is essential for high-resolution imaging. In general, when the value of the regularization coefficient η is large, the result of the deconvolution is too smooth, which leads to the weaker targets being ignored. On the contrary, the effect of noise cannot be suppressed, and a large number of bright spots appear on the image.

Typically, when dealing with the optimization problem shown in Eq. (31), a tendency is to limit the regularization coefficient $\eta \in (0, 1]$. However, for sonar imaging, due to the higher sparsity of the data model, we chose the regularization coefficient in the interval $(0, 2]$ instead of the traditional experience to obtain a faster convergence rate. Please note that the parameter range setting is based on numerous prior tests on imaging performance with different regularization parameters, proving that the range of $(0, 2]$ is applicable to underwater wideband coherent imaging and performs in a stable manner.

Regularization parameter optimization is a key issue that varies with experimental configuration conditions. Currently, there is no rigorous theoretical derivation to solve the optimization, so most methods use prior numerical information to select. A numerical difference method is applied to select the regularization coefficient η .³⁵ Consider the objective function of Eq. (31) as a function of the regularization coefficient η and denote it as

$$J(\eta) = \frac{1}{2} \|\mathbf{Y}_p \mathbf{E}_\eta - \mathbf{Y}\|_2^2 + \eta \|\mathbf{E}_\eta\|_1, \quad (37)$$

where \mathbf{E}_η denotes the solution of Eq. (31) obtained by iterating through the MFISTA at the corresponding value of η .

In this method, the value of η corresponding to the minimum of the second-order difference of Eq. (37) is taken as the value of the regularization coefficient, it is easier to calculate the second derivative, the optimization algorithm is very applicable, the mathematical expression is as follows:

$$\hat{\eta} = \arg \min_{\eta \in (0,2]} \Delta[\Delta J(\eta)], \quad (38)$$

where $\Delta(\cdot)$ denotes the first-order difference and $\hat{\eta}$ denotes the result of the selection of the regularization coefficient.

IV. SIMULATION ANALYSIS

In this section, the results of several simulations are presented to verify the performance of the proposed MT-MFISTA in sonar imaging. The CBF, RL, and NNLS algorithms are used as references to confirm that the algorithm has higher resolution and contrast results for wideband coherent signals with different SNRs. The imaging setup parameters are listed in Table I.

A. Regularization coefficient and number of iterations

In this simulation, we determine the value of the regularization coefficient η and the effect of the iterations on the performance of the proposed algorithm. Which is selected based on the principle of minimizing the norm according to Eq. (37). We consider two targets located at $[-1.5^\circ, 1.5^\circ]$. Setting the imaging angle to 130° and scanning at 0.5° intervals, using Eqs. (37) and (38), the variation of $\Delta[\Delta J(\eta)]$ with η can be obtained as in Fig. 3, where the minimum value represents the optimal parameter. It can be seen that $\Delta[\Delta J(\eta)]$ takes the minimum value when $\eta = 1.44$, which is used as the regularization coefficient of the MT-MFISTA in this paper subsequently. Here, the optimization step size of regularization parameter is sufficiently small to eliminate the significant impact of the parameter on the results. It is worth noting that since the curve in Fig. 3 is not smooth, in order to avoid significant impact on sonar imaging results due to human error, we conducted several numerical tests near the selected optimal value and found that that other suboptimal values can be selected with similar imaging results, but this may result in uncertainties in the beamforming performance.

The performance of the MT-MFISTA, RL, and NNLS algorithms with the number of iterations is given in Fig. 4. Perform 20 Monte Carlo experiments for each iteration and

TABLE I. The imaging setup parameters.

Parameter	Value
Number of array elements	64
Element spacing	2 mm
Signal form	LFM
Signal center frequency	350 kHz
Signal bandwidth	50 kHz
Pulse duration	50 μ s

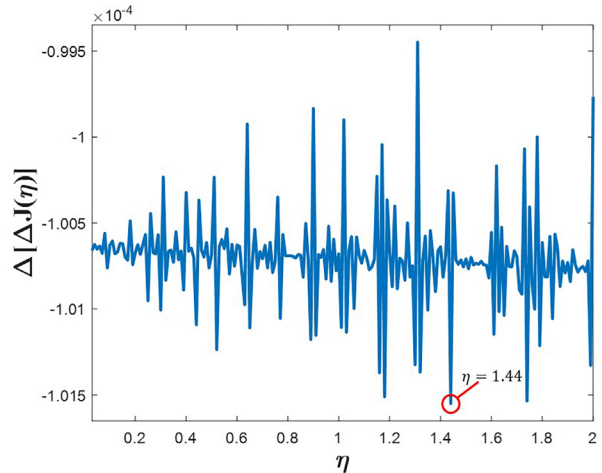


FIG. 3. The value of the regularization coefficient based on numerous *a priori* tests.

the CBF does not require an iterative process, which makes its performance metrics independent of the number of iterations. However, it is still carved out to make it easier to reflect the performance differences of different deconvolution algorithms. Please note that the simulation experiments are independent of the number of Monte Carlo experiments and represent the final convergence results. The performance parameters may undergo numerical changes due to variations in angle, array configuration, frequency, etc., but the overall trend and characteristics of the algorithm remain consistent. Figure 4(a) gives the variation of the mainlobe width with the iterations for different algorithms. It can be seen that compared to CBF, the MT-MFISTA, the RL and the NNLS algorithms decrease rapidly within a small number of iterations and then stabilize gradually with the number of iterations. Although the RL and the NNLS algorithms require fewer iterations than the MT-MFISTA to converge, they fail to achieve the same performance as the MT-MFISTA. The mainlobe width of the MT-MFISTA can be reduced to less than 1° at 200 iterations, which far exceeds the performance of others algorithms. Figure 4(b) shows the variation of the sidelobe level with the iterations, which broadly has the same trend as the main width comparison case. The difference is that the sidelobe level of the MT-MFISTA can be reduced to -30 dB, while the RL and NNLS algorithms are only around -18 and -16 dB, respectively. This is because the signals after the reflection of the targets are coherent, and the error caused by the model mismatch reduces the performance of the algorithms.

In summary, for the same number of iterations, the MT-MFISTA has better performance than the RL and the NNLS algorithms. In particular, it has excellent performances of narrower mainlobe width and lower sidelobe level. For the sake of the balance between algorithm performance and computational resources, in the next simulation experiments, we set $\eta = 1.44$ and the number of iterations is 200. Notice that these parameters are discussed specifically in

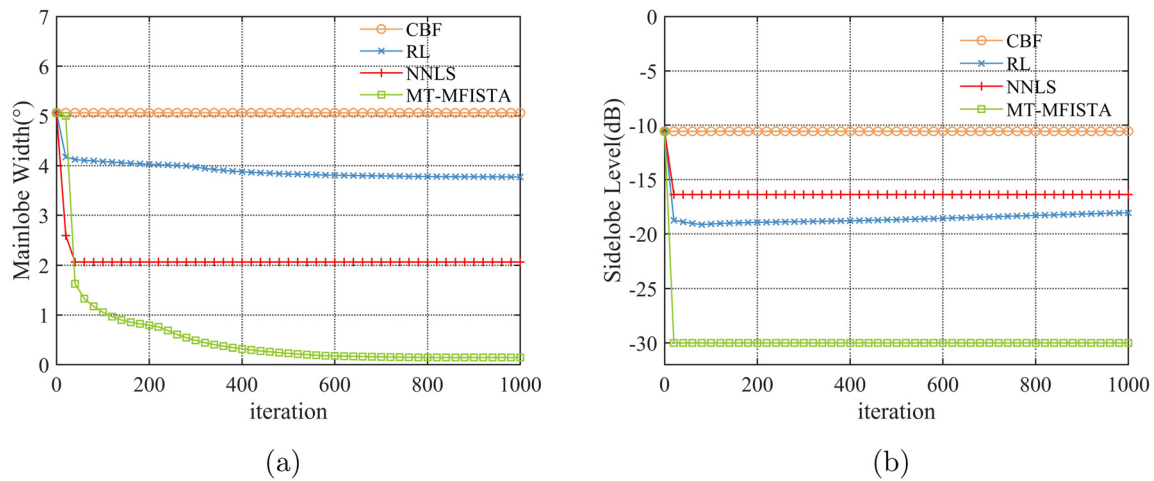


FIG. 4. The mainlobe width and the sidelobe level versus iteration number: (a) the mainlobe width, (b) the sidelobe level.

this paper, and other cases need to be adjusted to get better results.

B. Resolution performance for coherent targets

To demonstrate the superiority of MT-MFISTA, the resolution performance of CBF, RL, NNLS, and MT-MFISTA for coherent targets in different situations are

carried out. We establish a polar coordinate with the center of the receiver array as the origin, setting the imaging range to -65° to 65° .

First, there are two identical targets set at $(5 \text{ m}, 1.5^\circ)$ and $(5 \text{ m}, -1.5^\circ)$, respectively, and the SNR are all set to 10 dB. The imaging results of the proposed MT-MFISTA, CBF, RL, and NNLS are given in Fig. 5, and the results are

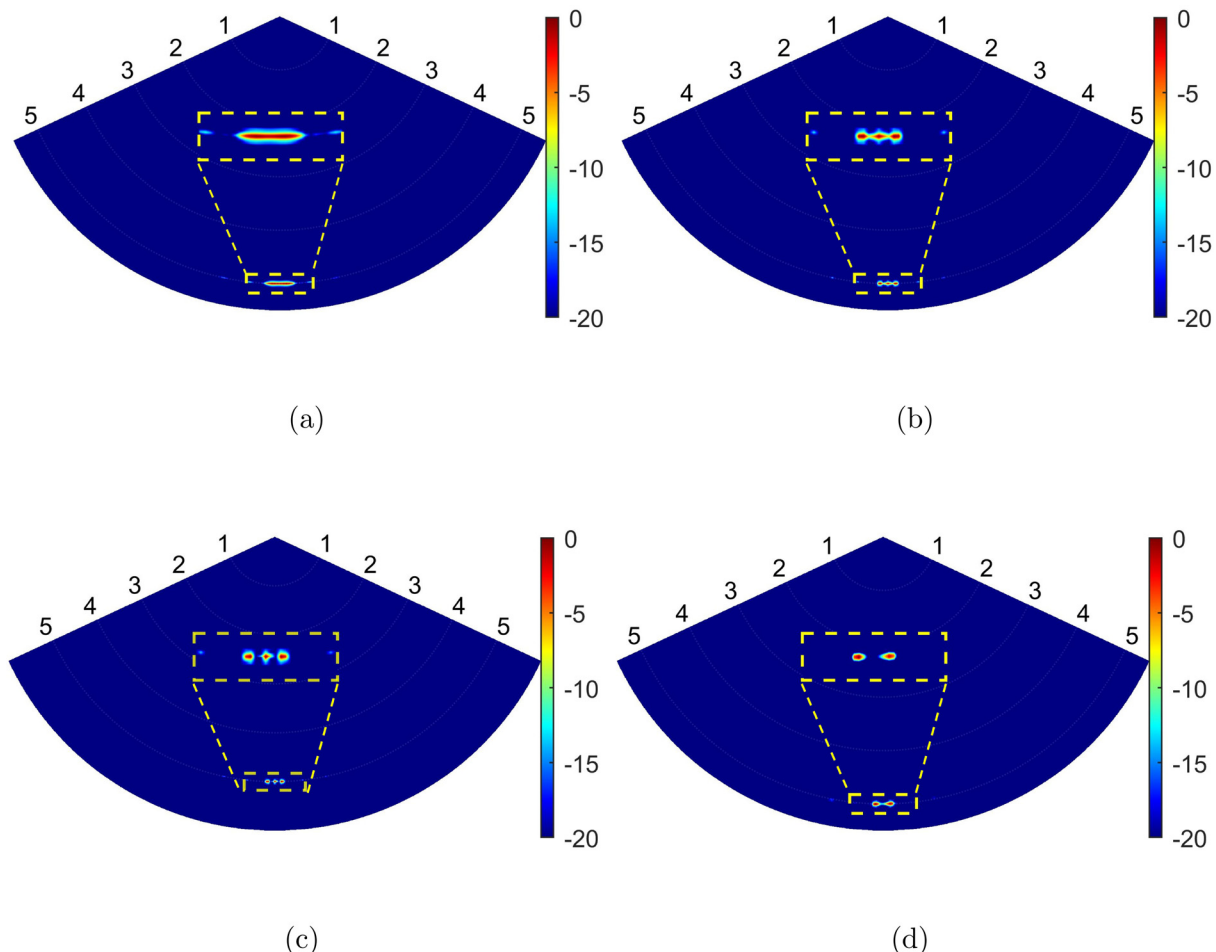


FIG. 5. The imaging results of coherent targets at $(5 \text{ m}, 1.5^\circ)$ and $(5 \text{ m}, -1.5^\circ)$: (a) CBF, (b) RL, (c) NNLS, (d) MT-MFISTA.

normalized with the ideal target intensity of 0 dB. We take the half-power beam width as the mainlobe width, and the highest sidelobe intensity as the sidelobe level. It can be seen from Fig. 5(a) that the targets are not correctly distinguished but merged their energies into a stronger one because of the poor resolution of the CBF. Thus, the CBF fails to get the true distribution of the targets when the targets are close and brings many high-intensity sidelobes. As shown in Figs. 5(b) and 5(c), although the RL and the NNLS have some performance improvement, they still cannot completely distinguish between two targets, which is because it cannot effectively suppress the cross term sidelobe, resulting in the appearance of a bright spot with comparable levels of the target intensity, and reducing the accuracy of the sonar image. On the contrary, the proposed MT-MFISTA performs deconvolution operations in the complex domain, thus circumventing the effect of cross term derived from intensity and matching the sonar imaging model better. Compared with others algorithms, the MT-MFISTA can completely discriminate between the two targets and has excellent suppression of sidelobes as shown in Fig. 5(d).

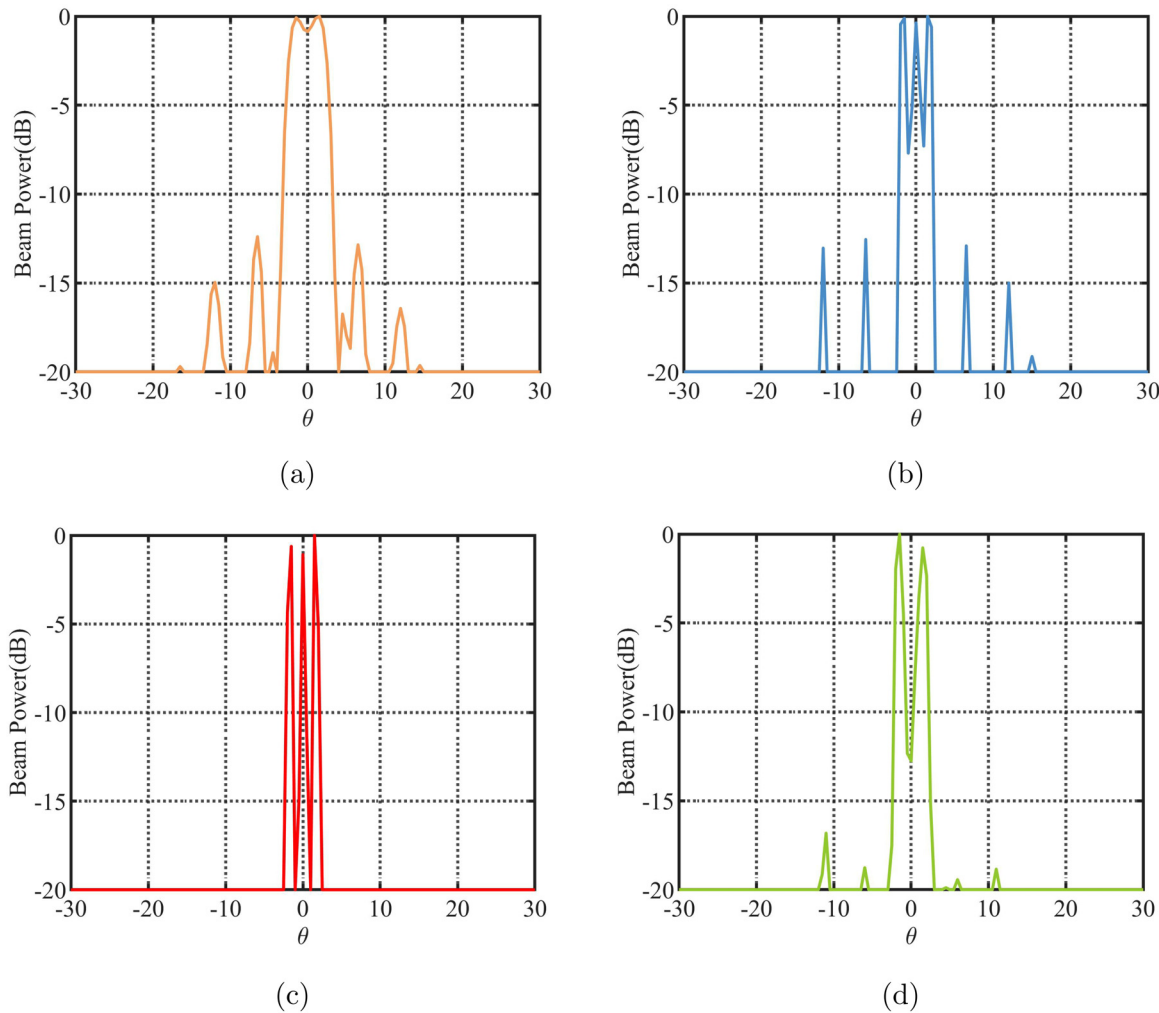


FIG. 6. The intensity slices of images at 5 m: (a) CBF, (b) RL, (c) NNLS, (d) MT-MFISTA.

To visually compare the detailed imaging results, we extract the intensity slices of the above images at the distance with 5 m in Fig. 6. The results show that the MT-MFISTA performs better compared to CBF, with the mainlobe width and sidelobe level of less than -15 dB and 1° , respectively. While the RL and NNLS algorithms also have the mainlobe width comparable to the MT-MFISTA, they suffer from the very high level of sidelobe between the two mainlobes. In addition, the RL and NNLS algorithms do not seem to suppress the sidelobes at other target positions either.

Second, to demonstrate the suitability of the proposed algorithm, we set the targets at different angles for the simulation experiment. Since the target position is symmetric at about 0° , we only show results at positive angles, but it has the same results for negative positions. The conditions are consistent with the above simulation, except that the locations of the targets are located at $(5\text{ m}, 8.5^\circ)$, $(5\text{ m}, 11.5^\circ)$, $(5\text{ m}, 18.5^\circ)$, and $(5\text{ m}, 21.5^\circ)$, respectively.

As can be seen from the results shown in Fig. 7, the MFISTA can clearly separate the two targets and has a strong suppression effect on sidelobes compared with the other algorithms. The results of CBF are given in Figs. 7(a)

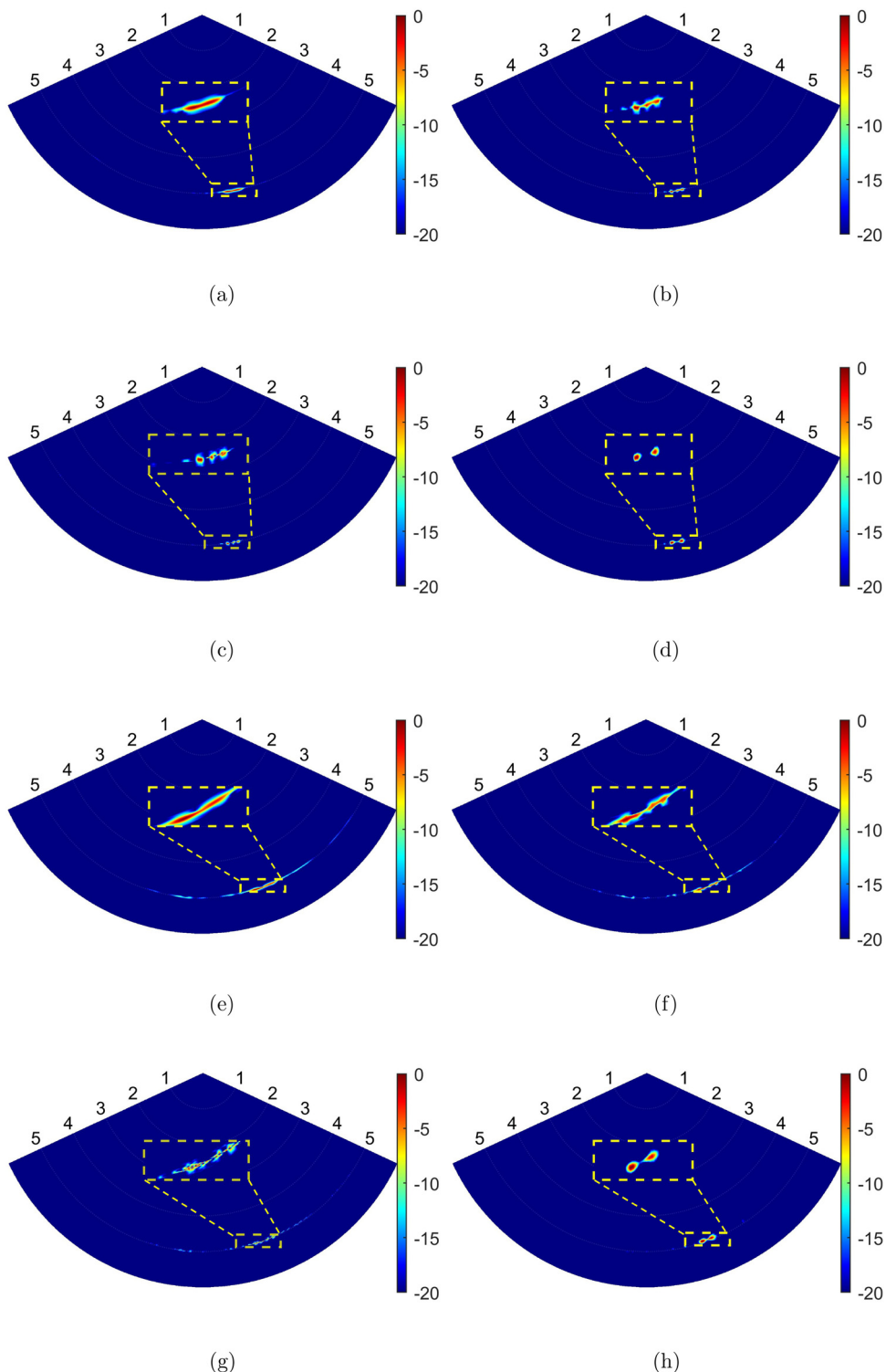


FIG. 7. The imaging results at (5 m, 8.5°), (5 m, 11.5°): (a) CBF, (b) RL, (c) NNLS, (d) MT-MFISTA, respectively. The imaging results at (5 m, 18.5°), (5 m, 21.5°): (e) CBF, (f) RL, (g) NNLS, (h) MT-MFISTA, respectively.

and 7(e), and it can be seen that the CBF algorithm consistently fails to separate the two targets, and the sidelobe level increases significantly as the target is shifted away from the center. As shown in Figs. 7(b) and 7(f), and Figs. 7(c) and 7(g), the RL and NNLS algorithms have some improved performance, but their resolution is always constrained by the

high intensity of the sidelobe produced by the cross term, and the sidelobe at other locations are elevated when the targets are farther off center.

The mainlobe width and sidelobe level of the different algorithms are compared in Table II, and the ranges are all set to 5 m. It can be seen that the mainlobe width of the CBF

TABLE II. The mainlobe width and the sidelobe level comparison of CBF, RL, NNLS, and MT-MFISTA.

Algorithms	(5 m, -1.5°), (5 m, 1.5°)		(5 m, 8.5°), (5 m, 11.5°)		(5 m, 18.5°), (5 m, 21.5°)	
	MW ^a ($^\circ$)	SL(dB) ^b	MW($^\circ$)	SL(dB)	MW($^\circ$)	SL(dB)
CBF	5.06	-11.94	5.14	-10.35	5.17	-10.90
RL	3.98	-13.01	3.96	-16.94	4.01	-10.00
NNLS	1.88	-13.04	2.04	-12.77	3.52	-3.6
MT-MFISTA	0.87	-15.15	0.77	-16.05	0.85	-15.75

^aMW represents mainlobe width.

^bSL represents sidelobe level.

algorithm is invariably wider than the target angular interval, and it has a relatively high sidelobe level. The RL and NNLS algorithms have the narrower mainlobe width, and but their sidelobe level remains high. The MT-MFISTA has an excellent performance in all locations, with a narrow mainlobe width that barely changes, and the sidelobe level is still about 5 dB lower than the CBF.

Finally, there are three clusters of targets at (4.5 m, 15°), (4.5 m, 18°), (5 m, -1.5°), (5 m, 1.5°), (5.5 m, -20°), and (5.5 m, -23°) to demonstrate the performance of the proposed algorithm in complex target scenarios. The results are given in Fig. 8, and it can be seen that similar to the above simulation results, the MT-MFISTA is still able to discriminate each target and has a better resolution than the

CBF, the RL and the NNLS algorithms. As shown in Figs. 8(a)–8(c), the CBF, RL, and NNLS algorithms are limited in resolution and cannot distinguish the targets. Figure 8(d) gives the results of the MT-MFISTA, where six targets are presented in the image.

C. Performance at different SNRs

To further verify the noise immunity of the proposed MT-MFISTA, a series of noises with different levels are added to the echo signals. We set the two targets at (5 m, -1.5°) and (5 m, 1.5°), respectively, and the random noise term follows a zero-mean Gaussian distribution. Figure 9 depicts the mainlobe width and sidelobe level relative to

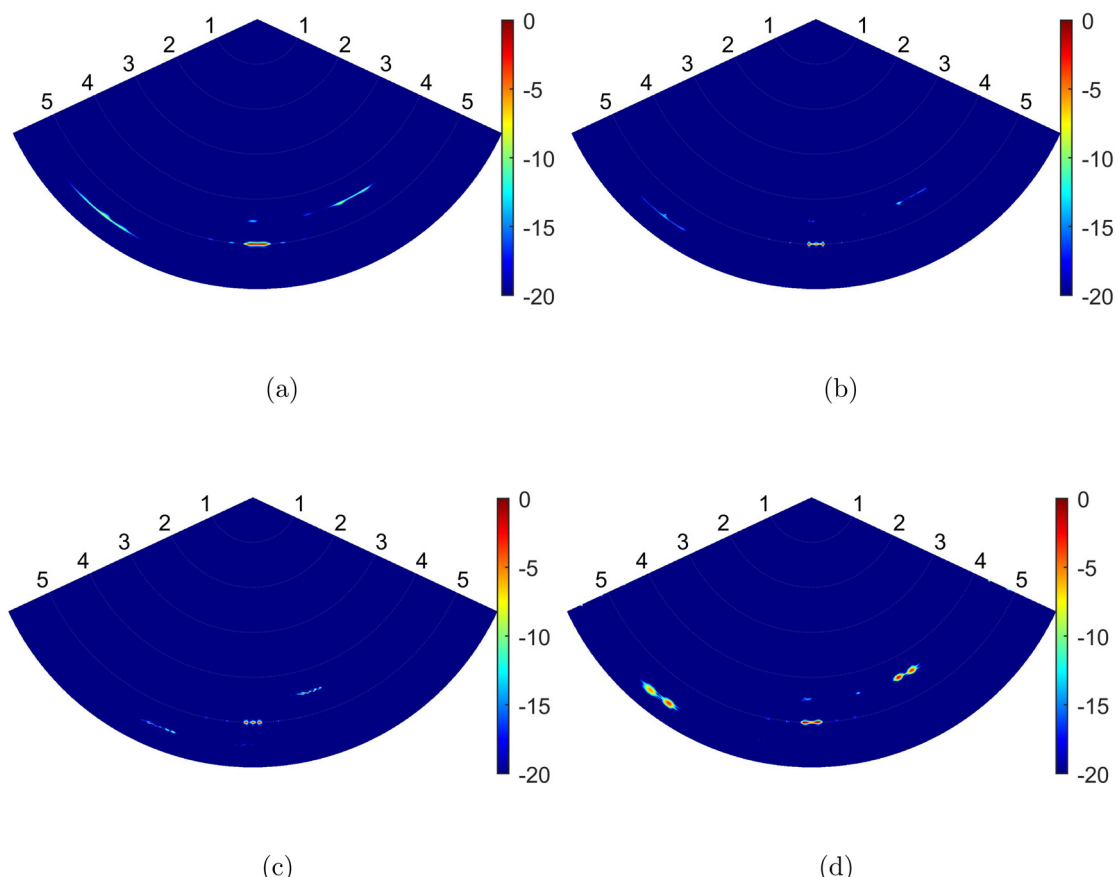


FIG. 8. The imaging results in complex target scenarios [six targets located at (4.5 m, 15°), (4.5 m, 18°), (5 m, -1.5°), (5 m, 1.5°), (5.5 m, -20°) and (5.5 m, -23°)]: (a) CBF, (b) RL, (c) NNLS, (d) MT-MFISTA.

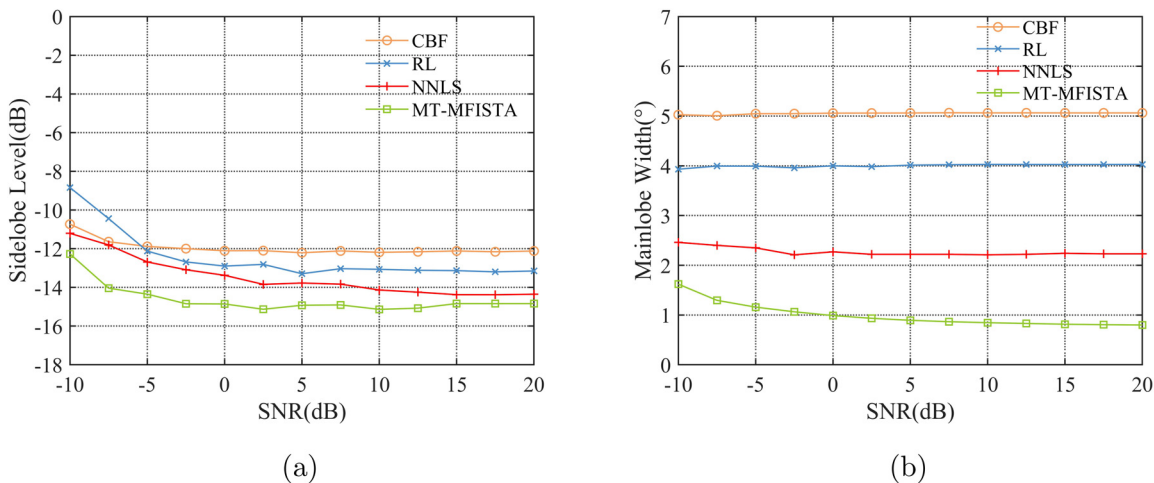


FIG. 9. The mainlobe width and the sidelobe level versus SNR: (a) the mainlobe width, (b) the sidelobe level.

the SNR. It can be seen that the MT-MFISTA, although its performance tends to decrease as the SNR decreases, outperforms the other algorithms in terms of mainlobe width and sidelobe level with the SNR values from -10 to 20 dB, which proves that the proposed algorithm has a better noise immunity to satisfy most environmental requirements. The results of the mainlobe width with SNR are shown in Fig. 9(a), where the MT-MFISTA has a tendency to increase in the mainlobe width when the SNR is below 0 dB and it rises to about 1.6° at -10 dB, but this is also narrower than the RL, NNLS, and CBF. When the SNR is higher than 10 dB, the mainlobe width of the MT-MFISTA is steadily reduced to about 0.8° , which is much better than that of the other methods. The variation of the sidelobe level with SNR is given in Fig. 9(b), and it can be seen that the suppression of the sidelobe decreases below 0 dB for the four algorithms, but MT-MFISTA still has the lowest sidelobe height. When the SNR is greater than 0 dB, the sidelobe level of the MT-MFISTA stabilizes at -15 dB, which is about 4 dB lower than the CBF.

V. EXPERIMENTAL RESULTS

In this section, we conducted practical experiments in Jingye Lake, located in Tianjin, China, to verify the effectiveness of the proposed algorithm. After the actual measurement, the average depth of the lake is about 5 m, which is a complex experimental environment with strong background noise and interface reflection interference, but fortunately, simulation analyses have already verified that the performance of this algorithm remains stable when $\text{SNR} = -10$ dB. The sound speed is 1480.01 m s^{-1} , and the experimental scene is shown in Fig. 10. The tire was placed in water with two stones behind it as the main detection targets for this experiment, which is more compatible with actual imaging scenarios and better highlights the imaging performance.

We developed a lab-built imaging sonar system for this experimental performance tests, and the receiver array is a

uniform linear array, in which the number of elements was 64 and the spacing was 0.600 mm. The imaging sonar system was placed at a depth of 1 m and looked forward from a perspective approximately parallel to the lake's surface. The imaging area has a maximum detection distance of 5 m and a horizontal angle coverage of 160° with a scanning interval of 0.5° . This imaging sonar system consists of a transceiver transducer array, a wideband signal module, and a signal processing circuit, which is shown in Fig. 11.

The imaging coverage is divided from -80° to 80° in the horizontal direction, and the results are normalized with the highest intensity of 0 dB. The experimental results are shown in Fig. 12, and we can see that there is a high-intensity arc at a distance of 1 m in the image. This is due to the sonar itself and is not a real target. To easily compare the results of different algorithms, we locally zoom in on the

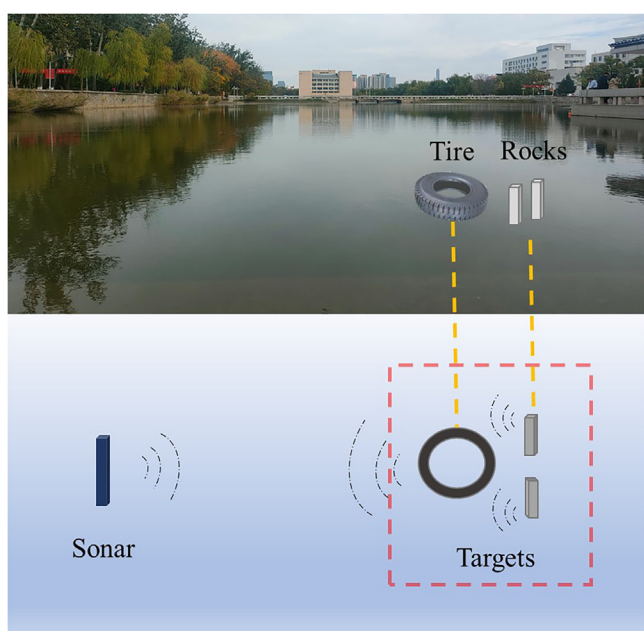


FIG. 10. The test environment of imaging sonar performance.



FIG. 11. A lab-built imaging sonar system.

target region. Generally, the proposed algorithm has higher resolution and contrast, and is able to clearly present the target contours and detailed features. The imaging result of the CBF is shown in Fig. 12(a), and it is clear that the CBF imaging performance is unsatisfactory for both the boundary line and the target region, which is due to wide mainlobe and high-intensity sidelobe of the algorithm. Figure 12(b) gives the result of the RL algorithm, and it can be seen that although the RL algorithm has a better effect on the target contour boundaries, it is hardly able to carve the tire detail features of the imaging region. The imaging result of the NNLS is shown in Fig. 12(c) and it is difficult to distinguish the targets in the image. This is because the RL and NNLS algorithms, when the imaging objects are relevant targets, produces a high-intensity sidelobe because of the effect of

cross-terms, drowning the important targets as well as detailed features in the background.

Subsequently, the imaging results of the MT-MFISTA are presented in Fig. 12(d). Compared to the CBF, RL, and NNLS, the proposed algorithm provides a notable improvement for both the boundary lines and the target region. The MT-MFISTA can clearly render the outline of the tire and distinguish detailed feature between two rocks, which cannot be achieved by both CBF and RL algorithms. Additionally, the image offers higher contrast, thanks to the suppression of the sidelobe by the MT-MFISTA.

VI. CONCLUSION

This study proposed an MT-MFISTA method to improve the resolution of imaging sonar in the presence of coherent targets. The MFISTA was developed in the complex domain to solve the imaging challenge of coherent echo interference, and the matrix transform was applied to solve the beamforming problem of wideband signals. The combined methods accurately establish the high-resolution imaging model. The simulation and experimental results for a ULA revealed that the MT-MFISTA has a superior mainlobe width and sidelobe level compared to the CBF, RL, and NNLS algorithms. In the same simulation cases, the mainlobe width of the MT-MFISTA is less than 1° , which is much smaller than that of the CBF, RL, and NNLS. Moreover, the MT-MFISTA also showed excellent performance at low SNR and always separates the targets better than the other algorithms.

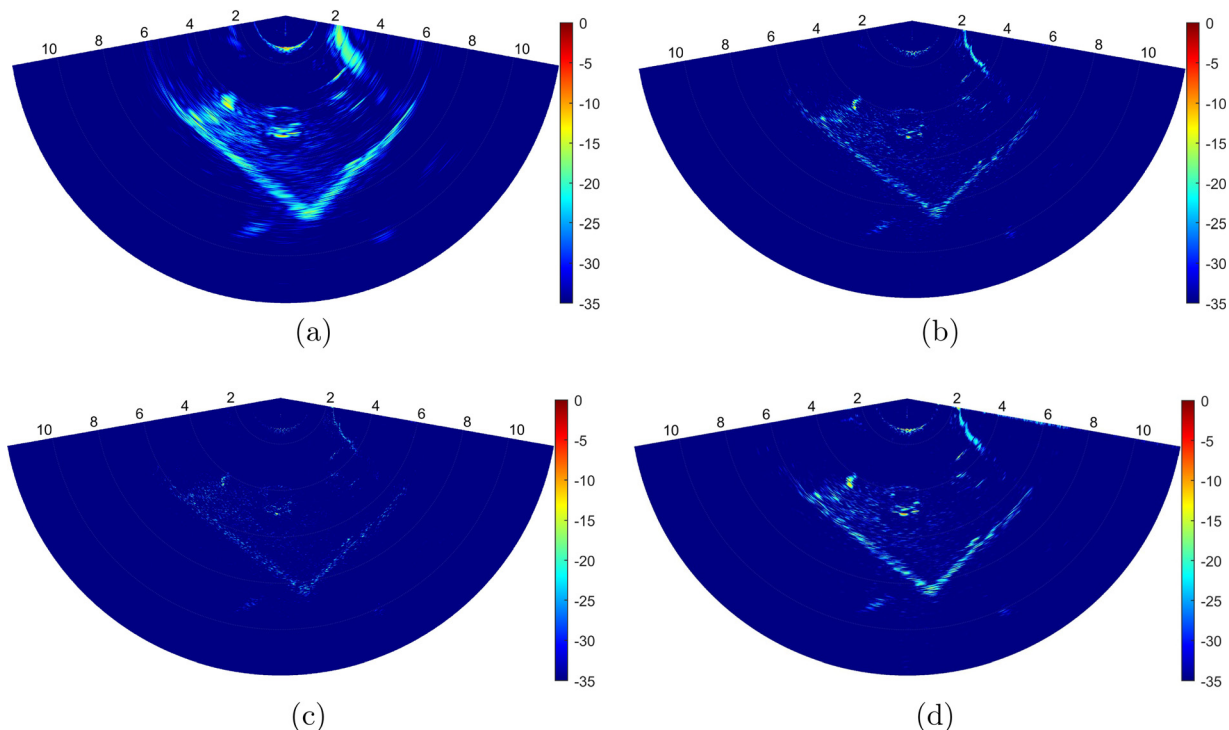


FIG. 12. Imaging results of different algorithms under lake testing conditions: (a) CBF, (b) RL, (c) NNLS, (d) MT-MFISTA.

Further, compared with intensity-based deconvolutions, this MT-MFISTA avoids the coherence associated with the square of the energy spectrum by performing deconvolution processing in the complex domain. Thus, it is applicable to ocean acoustics related to coherent array signal processing, such as underwater acoustic positioning, imaging, and communication, especially concerning high-performance DOA estimation. In subsequent work, further research will be needed to investigate whether this MT-MFISTA method can achieve high performance when the application scenario involves weak sparsity, severe Doppler effects, and strong reverberation. The adaptive variation of hyperparameters will be studied to improve the computational efficiency and adaptability.

ACKNOWLEDGMENTS

This work was supported by the National Natural Science Foundation of China (Grant Nos. 52401409 and 52371352), State Key Laboratory of Acoustics and Marine Information (Grant No. SKLA202407), the Opening Fund of National Key Laboratory of Underwater Acoustic Technology (Grant No. SSKF202407), and Key Laboratory of Marine Environmental Information Technology, Ministry of Natural Resources (Grant No. 2023E7-0081).

AUTHOR DECLARATIONS

Conflict of Interest

We declare that we do not have any commercial or associative interest that represents a conflict of interest in connection with the work submitted.

DATA AVAILABILITY

The data that support the findings of the present study are available from the corresponding author upon reasonable request.

- ¹Z. Yan, X. Min, D. Xu, and D. Geng, “A novel method for underactuated UUV tracking unknown contour based on forward-looking sonar,” *Ocean Eng.* **301**, 117545 (2024).
- ²H. Tan, L. Zheng, C. Ma, Y. Xu, and Y. Sun, “Deep learning-assisted high-resolution sonar detection of local damage in underwater structures,” *Autom. Constr.* **164**, 105479 (2024).
- ³M. Ho, S. El-Borgi, D. Patil, and G. Song, “Inspection and monitoring systems subsea pipelines: A review paper,” *Struct. Health Monit.* **19**(2), 606–645 (2020).
- ⁴L. Bjørnø, “Developments in sonar and array technologies,” in *2011 IEEE Symposium on Underwater Technology and Workshop on Scientific Use of Submarine Cables and Related Technologies* (IEEE, New York, 2011), pp. 1–11.
- ⁵W. Liu, M. Haardt, M. S. Greco, C. F. Mecklenbräuker, and P. Willett, “Twenty-five years of sensor array and multichannel signal processing: A review of progress to date and potential research directions,” *IEEE Signal Process. Mag.* **40**(4), 80–91 (2023).
- ⁶J. Capon, “High-resolution frequency-wavenumber spectrum analysis,” *Proc. IEEE* **57**(8), 1408–1418 (1969).
- ⁷R. Schmidt, “Multiple emitter location and signal parameter estimation,” *IEEE Trans. Antennas Propag.* **34**(3), 276–280 (1986).
- ⁸W. Zhang, Y. Han, M. Jin, and X. Qiao, “Multiple-Toeplitz matrices reconstruction algorithm for DOA estimation of coherent signals,” *IEEE Access* **7**, 49504–49512 (2019).

- ⁹A. E. A. Blomberg, A. Austeng, and R. E. Hansen, “Adaptive beamforming applied to a cylindrical sonar array using an interpolated array transformation,” *IEEE J. Oceanic Eng.* **37**(1), 25–34 (2012).
- ¹⁰J. I. Buskenes, R. E. Hansen, and A. Austeng, “Low-complexity adaptive sonar imaging,” *IEEE J. Oceanic Eng.* **42**(1), 87–96 (2016).
- ¹¹Y. Yue, C. Zhou, F. Xing, K.-K. R. Choo, and Z. Shi, “Adaptive beamforming for cascaded sparse diversely polarized planar array,” *IEEE Trans. Veh. Technol.* **72**(12), 15648–15664 (2023).
- ¹²P. Gerstoft, A. Xenaki, and C. F. Mecklenbräuker, “Multiple and single snapshot compressive beamforming,” *J. Acoust. Soc. Am.* **138**(4), 2003–2014 (2015).
- ¹³T. F. Brooks and W. M. Humphreys, “A deconvolution approach for the mapping of acoustic sources (DAMAS) determined from phased microphone arrays,” *J. Sound Vib.* **294**(4–5), 856–879 (2006).
- ¹⁴K. Ehrenfried and L. Koop, “Comparison of iterative deconvolution algorithms for the mapping of acoustic sources,” *AIAA J.* **45**(7), 1584–1595 (2007).
- ¹⁵J. Tsao and B. D. Steinberg, “Reduction of sidelobe and speckle artifacts in microwave imaging: The CLEAN technique,” *IEEE Trans. Antennas Propag.* **36**(4), 543–556 (1988).
- ¹⁶W. H. Richardson, “Bayesian-based iterative method of image restoration,” *J. Opt. Soc. Am.* **62**(1), 55–59 (1972).
- ¹⁷T. Yang, “Deconvolved conventional beamforming for a horizontal line array,” *IEEE J. Oceanic Eng.* **43**(1), 160–172 (2018).
- ¹⁸D. Sun, C. Ma, J. Mei, W. Shi, and L. Gao, “The deconvolved conventional beamforming for non-uniform line arrays,” in *2018 OCEANS-MTS/IEEE Kobe Techno-Oceans (OTO)* (IEEE, New York, 2018), pp. 1–4.
- ¹⁹D. Sun, C. Ma, T. Yang, J. Mei, and W. Shi, “Improving the performance of a vector sensor line array by deconvolution,” *IEEE J. Oceanic Eng.* **45**(3), 1063–1077 (2020).
- ²⁰T. Yang, “Performance analysis of superdirective of circular arrays and implications for sonar systems,” *IEEE J. Oceanic Eng.* **44**(1), 156–166 (2019).
- ²¹Z. Ye and T. Yang, “Deconvolved conventional beamforming for a coprime array,” in *OCEANS 2019-Marseille* (IEEE, New York, 2019), pp. 1–6.
- ²²J. Huang, T. Zhou, W. Du, J. Shen, and W. Zhang, “Smart ocean: A new fast deconvolved beamforming algorithm for multibeam sonar,” *Sensors* **18**(11), 4013 (2018).
- ²³C. Ma, L. Liu, Q. Wang, W. Zhang, and X. Liu, “High-performance deep-sea long-range underwater acoustic communication: Deconvolved conventional beamforming based approach,” *Phys. Commun.* **64**, 102339 (2024).
- ²⁴D. Sun, C. Ma, J. Mei, and W. Shi, “Improving the resolution of underwater acoustic image measurement by deconvolution,” *Appl. Acoust.* **165**, 107292 (2020).
- ²⁵P. Wang, C. Chi, J. Liu, and H. Huang, “Improving performance of three-dimensional imaging sonars through deconvolution,” *Appl. Acoust.* **175**, 107812 (2021).
- ²⁶X. Liu, J. Fan, C. Sun, Y. Yang, and J. Zhuo, “Deconvolving range profile for sonar imaging using stepped-frequency LFM pulses,” *IEEE Geosci. Remote Sens. Lett.* **18**(6), 954–958 (2021).
- ²⁷X. Liu, J. Fan, C. Sun, Y. Yang, and J. Zhuo, “High-resolution and low-sidelobe forward-look sonar imaging using deconvolution,” *Appl. Acoust.* **178**, 107986 (2021).
- ²⁸C. Ma, D. Sun, J. Mei, and T. Teng, “Spatiotemporal two-dimensional deconvolution beam imaging technology,” *Appl. Acoust.* **183**, 108310 (2021).
- ²⁹X. Liu, Y. Yang, C. Sun, J. Zhuo, Y. Wang, and Q. Zhai, “High-angular-and range-resolution imaging using MIMO sonar with two-dimensional deconvolution,” *IET Radar. Sonar Navig.* **17**(6), 991–1001 (2023).
- ³⁰Z. Chu and Y. Yang, “Comparison of deconvolution methods for the visualization of acoustic sources based on cross-spectral imaging function beamforming,” *Mech. Syst. Sig. Process.* **48**(1–2), 404–422 (2014).
- ³¹J. Fan, Q. Tao, Z. Qian, and X. Fu, “Underwater wideband coherent signals DOA estimation using sparse representation and deconvolution,” *Meas. Sci. Technol.* **35**(6), 065023 (2024).
- ³²F. Wang, X. Tian, X. Liu, B. Gu, F. Zhou, and Y. Chen, “Combination complex-valued Bayesian compressive sensing method for sparsity constrained deconvolution beamforming,” *IEEE Trans. Instrum. Meas.* **71**, 9506013 (2022).
- ³³S. Jiang, R. Jiang, X. Liu, B. Gu, and Y. Chen, “Probability-based complex-valued fast iterative shrinkage-thresholding algorithm for deconvolution beamforming,” *IEEE J. Oceanic Eng.* **49**(2), 340–351 (2024).
- ³⁴F. Ma and X. Zhang, “Wideband DOA estimation based on focusing signal subspace,” *Signal, Image Video Process.* **13**, 675–682 (2019).
- ³⁵S.-J. Kim, K. Koh, M. Lustig, S. Boyd, and D. Gorinevsky, “An interior-point method for large-scale ℓ_1 -regularized least squares,” *IEEE J. Sel. Top. Signal Process.* **1**(4), 606–617 (2007).